

Probabilistic 3-D time-lapse inversion of magnetotelluric data: application to an enhanced geothermal system

M. Rosas-Carbajal,^{1,*} N. Linde,¹ J. Peacock,² F.I. Zyserman,³ T. Kalscheuer^{4,†} and S. Thiel^{5,‡}

¹Applied and Environmental Geophysics Group, University of Lausanne, Switzerland. E-mail: Marina.Rosas@Unil.ch

²US Geological Survey, Menlo Park, California, USA

³CONICET - Facultad de Ciencias Astronómicas y Geofísicas, Universidad Nacional de La Plata, Argentina

⁴Institute of Geophysics, ETH Zurich, Switzerland

⁵University of Adelaide, South Australia, Australia

Accepted 2015 September 21. Received 2015 September 2; in original form 2014 December 2

SUMMARY

Surface-based monitoring of mass transfer caused by injections and extractions in deep boreholes is crucial to maximize oil, gas and geothermal production. Inductive electromagnetic methods, such as magnetotellurics, are appealing for these applications due to their large penetration depths and sensitivity to changes in fluid conductivity and fracture connectivity. In this work, we propose a 3-D Markov chain Monte Carlo inversion of time-lapse magnetotelluric data to image mass transfer following a saline fluid injection. The inversion estimates the posterior probability density function of the resulting plume, and thereby quantifies model uncertainty. To decrease computation times, we base the parametrization on a reduced Legendre moment decomposition of the plume. A synthetic test shows that our methodology is effective when the electrical resistivity structure prior to the injection is well known. The centre of mass and spread of the plume are well retrieved. We then apply our inversion strategy to an injection experiment in an enhanced geothermal system at Paralana, South Australia, and compare it to a 3-D deterministic time-lapse inversion. The latter retrieves resistivity changes that are more shallow than the actual injection interval, whereas the probabilistic inversion retrieves plumes that are located at the correct depths and oriented in a preferential north–south direction. To explain the time-lapse data, the inversion requires unrealistically large resistivity changes with respect to the base model. We suggest that this is partly explained by unaccounted subsurface heterogeneities in the base model from which time-lapse changes are inferred.

Key words: Inverse theory; Probability distributions; Non-linear electromagnetics; Hydrogeophysics.

1 INTRODUCTION

Monitoring of subsurface mass transfer is critical to maximize oil, gas and geothermal production to improve groundwater remediation and to manage environmental risk. In particular, enhanced geothermal systems, which constitute an attractive and increasingly studied renewable energy source (Muñoz 2014), require information on the flow paths taken by the injected water in order to subsequently recover it and use it for energy production.

Geophysical methods are suitable to characterize subsurface processes, both because of their non-invasive nature and their capacity to provide spatially extensive data coverage (e.g. Hubbard & Rubin 2005). Various geophysical techniques have been applied in time-lapse studies that aim at inferring temporal changes in the near subsurface (e.g. LaBrecque & Yang 2001; Day-Lewis *et al.* 2002; Ajo-Franklin *et al.* 2007; Miller *et al.* 2008; Doetsch *et al.* 2010; Rosas Carbajal *et al.* 2012). Tailored inverse formulations that reduce noise and model parametrizations that focus on temporal changes make time-lapse inversions more suitable than simple differencing of models obtained from separate inversions. LaBrecque & Yang (2001) proposed a time-lapse difference inversion and applied it to 3-D electrical resistivity tomography (ERT) data. A similar strategy was applied by Ajo-Franklin *et al.* (2007) to better resolve subsurface variations related to CO₂ injection with crosshole

*Now at: Institut de Physique du Globe de Paris, France.

†Now at: Department of Earth Sciences, Uppsala University, Sweden.

‡Now at: Geological Survey of South Australia, Australia.

seismics, and by Doetsch *et al.* (2010) combined with joint inversion of crosshole ERT and ground-penetrating radar (GPR). More recently, Rosas Carbajal *et al.* (2012) applied this type of inversion approach to time-lapse electromagnetic (EM) data, specifically radio magnetotelluric (RMT) and audio magnetotelluric (AMT). Inspired by the work of Falgàs *et al.* (2009), who monitored saltwater intrusion in a coastal aquifer, Rosas Carbajal *et al.* (2012) demonstrated significant improvements in the resulting models by incorporating information about the expected temporal changes in the subsurface and by removing systematic errors.

For deeper targets, for example in volcanic and geothermal studies, microseismic and EM methods represent prominent monitoring tools. The former consists in locating natural (e.g. Brenguier *et al.* 2007, 2008) or induced (e.g. House 1987) seismic sources associated with fracture openings caused by hydraulic pressure variation. The latter are sensitive to changes in electrical resistivity, which can be related to fluid redistributions and changes in fracture connectivity. Feasibility studies that focused on marine (e.g. Lien & Manneth 2008; Orange *et al.* 2009) and on-land (Wirianto *et al.* 2010) controlled source electromagnetics (CSEM) showed that monitoring is feasible, but complicated by the diffusive character of the EM fields and the large depths of investigation. On-land CSEM has some disadvantages with respect to marine applications, for example, the need for large source–receiver distances, with kilometre-long sources that need to be accurately modelled (Constable 2010; Streich & Becken 2011). Recent advances (e.g. Grayver *et al.* 2014) suggest that monitoring of resistive targets will soon become feasible. Bedrosian *et al.* (2004) performed one of the first magnetotelluric (MT) studies aimed at monitoring a fluid injection experiment. They conducted 2-D inversions to map the subsurface resistivity changes following the injection, but no changes could be detected due to the low signal-to-noise-ratio. Kappler *et al.* (2010) studied MT data variations over a period of 4 yr at the San Andreas Fault and showed that no significant EM signal precursors occurred prior to the most significant earthquake event during this period. Aizawa *et al.* (2011) conducted a one-year monitoring study at a volcano in Japan using two MT stations. The data indicate large temporal changes, and the 2-D inversion models suggested that the resistivity changes occurred at the sea level. Peacock *et al.* (2012, 2013) presented MT monitoring results of an injection experiment in an enhanced geothermal system at Paralana, Australia. In this experiment, 3100 m³ of saline water, together with acids, were injected at 3.7 km depth to stimulate the opening of new fractures and enable remote monitoring of the plume. The authors observed changes above the ambient noise in both apparent resistivity and phase at ~50 MT stations, with maximum changes occurring in the north–northeast direction. No attempts were made to invert these data.

The works cited above present deterministic approaches to the inverse problem, where one single subsurface model that explains the data is sought by iterative linearization and regularization, and no formal estimates of model parameter uncertainty are made. Probabilistic inversion (e.g. Mosegaard & Tarantola 1995; Tarantola 2005) offers an alternative approach by estimating the posterior probability density function (pdf) of the model parameters, which contains detailed information about parameter uncertainty. To numerically estimate the posterior distributions, Markov chain Monte Carlo (MCMC) simulation methods are often used. These methods are able to (e.g. Sambridge & Mosegaard 2002, and references therein) (1) correctly treat non-linear relationships between models and data, (2) successfully converge to the posterior pdf of the model parameters, and thus, (3) adequately characterize parameter uncertainty. Pioneering EM applications of probabilistic inversions

were performed by Tarits *et al.* (1994), Grandis *et al.* (1999, 2002), Hou *et al.* (2006), Khan *et al.* (2006) and Chen *et al.* (2007). The computational costs of the algorithms, which require many evaluations of the forward response, have only recently been overcome to explore high dimensional problems: Chen *et al.* (2012) presented an MCMC algorithm to invert 2-D MT data based on a fixed number of layers, and Rosas-Carbajal *et al.* (2014) presented the first 2-D pixel-based MCMC inversion of plane-wave EM data. Probabilistic inversions have been applied to time-lapse geophysical data (e.g. Ramirez *et al.* 2005; Laloy *et al.* 2012; Lochbühler *et al.* 2014). Of particular interest in this study is the work by Laloy *et al.* (2012), who inverted synthetic crosshole GPR traveltime data to characterize an injected water plume in partially saturated media. The authors proposed a model parametrization based on the Legendre moments of the injected plume. This reduces the number of parameters to estimate, and thus the computation time, and constrains the solutions to those that honour the total volume of water injected.

In this paper, we address the problem of estimating the mass transfer following a deep injection with time-lapse MT data. To do so, we present the first deterministic and probabilistic 3-D time-lapse inversions of MT data. We parametrize the probabilistic inversion using a Legendre moment decomposition similar to Laloy *et al.* (2012), but under saturated conditions and for a saline fluid, and provide uncertainty estimates of the plume's centre of mass and spread. After a numerical test, we focus on the plume resulting from the Paralana injection experiment (Peacock *et al.* 2012) and compare the MCMC inversion results to those obtained by time-lapse deterministic inversion.

2 METHODOLOGY

2.1 Probabilistic inversion

We use a probabilistic framework to estimate the posterior pdf of a set of model parameters that describe a tracer plume at a given time-lapse t . Let this system be described by a vector of B model parameters, $\mathbf{b}_t = (b_{1,t}, b_{2,t}, \dots, b_{B,t})$ and a set of N observations, $\mathbf{d}_t = (d_{1,t}, d_{2,t}, \dots, d_{N,t})$, which are related to \mathbf{b}_t via a set of equations,

$$\mathbf{d}_t = g(\mathbf{b}_t) + \mathbf{e}_{r,t} + \mathbf{e}_{\text{sys}}, \quad (1)$$

where $g(\mathbf{b}_t)$ is the simulated MT forward response, $\mathbf{e}_{r,t}$ is a random observational error that is varying in time and \mathbf{e}_{sys} is a systematic contribution that is present at all times. The latter may include static shifts, errors in sensor calibrations and/or geometrical errors (e.g. station positioning). The posterior pdf $p(\mathbf{b}_t|\mathbf{d}_t)$ of the model parameters conditional on the data is found by applying Bayes theorem (e.g. Tarantola & Valette 1982). In the case of a fixed model parametrization, this results in the following proportionality equality

$$p(\mathbf{b}_t|\mathbf{d}_t) \propto p(\mathbf{b}_t)L(\mathbf{b}_t). \quad (2)$$

The prior probability, $p(\mathbf{b}_t)$, represents the information known about the subsurface before collecting the actual data, whereas the likelihood function, $L(\mathbf{b}_t)$, describes the likelihood that a given model is responsible for the observed data. The larger the likelihood, the closer the model response is to the experimental data. Typically, the assumption is made that the errors are uncorrelated and follow a normal distribution with zero mean. Then the log-likelihood

function, that is, the logarithm of the likelihood function $l(\mathbf{b}_t)$, is proportional to $-\frac{1}{2}\varphi_{l_2}$, where

$$\varphi_{l_2} = \sum_{i=1}^N \left(\frac{g_i(\mathbf{b}_t) - d_{i,t}}{\sigma_{i,t}} \right)^2, \quad (3)$$

represents the data misfit, $\sigma_{i,t}$ denotes the standard deviation of the i th error at time t and the subscript l_2 indicates the l_2 -norm. Under these assumptions, φ_{l_2} is expected to follow a chi-squared distribution with expected value N . A common representation of the data misfit is the root mean square (RMS) misfit:

$$\text{RMS} = \sqrt{\frac{1}{N} \sum_{i=1}^N \left(\frac{g_i(\mathbf{b}_t) - d_{i,t}}{\sigma_{i,t}} \right)^2}, \quad (4)$$

which attains the value of $\text{RMS} = 1$ when $\varphi_{l_2} = N$.

When the data errors contain significant outliers, it is often better to use an exponential distribution, which is equivalent to using an l_1 -norm instead of an l_2 -norm to describe the data misfit (Menke 1989). The l_1 -norm is more robust and often represents a more realistic description of data errors (e.g. Claerbout & Muir 1973; Egbert & Booker 1986; Chave & Thomson 1989; Farquharson & Oldenburg 1998; Tarantola 2005). For uncorrelated errors, the corresponding log-likelihood function is proportional to $-\varphi_{l_1}$, where the data misfit is now defined as

$$\varphi_{l_1} = \sum_{i=1}^N \left| \frac{g_i(\mathbf{b}_t) - d_{i,t}}{\sigma_{i,t}} \right|, \quad (5)$$

and $\sigma_{i,t}$ represents the mean deviation of the i th error at time t (e.g. Tarantola 2005).

To numerically implement the probabilistic inversion, we use the DREAM_(ZS) algorithm (Laloy & Vrugt 2012). This is an adaptive MCMC algorithm (e.g. Roberts & Rosenthal 2007) which, in order to render the sampling more efficient, runs multiple chains in parallel and implements sampling from an archive of past states. Jumps in each chain are obtained by computing the difference between one or multiple pairs of chain states, drawn from an external sample of points that summarizes the search history of all the individual chains. A proposed model $\mathbf{b}_{t,\text{new}}$ is accepted, in the case of a uniform prior, with probability (e.g. Mosegaard & Tarantola 1995):

$$P_{\text{accept}} = \min \{1, \exp[l(\mathbf{b}_{t,\text{new}}) - l(\mathbf{b}_{t,\text{old}})]\}, \quad (6)$$

where $\mathbf{b}_{t,\text{old}}$ is the chain's last accepted model. If the proposal is accepted then the chain moves to $\mathbf{b}_{t,\text{new}}$, otherwise the chain remains at its old location. After a burn-in period, the sampled model realizations are distributed according to the underlying posterior distribution. To assess convergence, the Gelman–Rubin statistic (Gelman & Rubin 1992) is periodically computed using the last 50 per cent of the chains' samples. Convergence to a limiting distribution is declared if the Gelman–Rubin statistic is less than 1.2 for all model parameters.

A variation of the DREAM_(ZS) algorithm is the so-called MT-DREAM_(ZS) algorithm (Laloy & Vrugt 2012), which has recently been applied to several types of geophysical data such as GPR, RMT and ERT (Laloy *et al.* 2012; Linde & Vrugt 2013; Lochbühler *et al.* 2014; Rosas-Carbajal *et al.* 2014). This multiple-try sampling procedure, designed for high parameter dimensions (i.e., more than ~ 30 model parameters), proposes several model variations per chain and per realization, and thus requires many forward computations running in parallel to be efficient. In the present contribution we use DREAM_(ZS) as we estimate at maximum 14 parameters. We run the different chains in parallel and use parallelized forward solvers.

2.2 Time-lapse strategy

Rosas Carbajal *et al.* (2012) proposed a time-lapse inversion to derive temporal changes from an initial 2-D resistivity model using time-lapse RMT and AMT data. The strategy is based on data differencing (LaBrecque & Yang 2001) to remove systematic errors (see eq. 1). Although the examples were limited to the audio and radio frequency range, this strategy is directly applicable to other types of geophysical data, in particular MT data.

First, a base resistivity model is obtained by means of a deterministic inversion using the data acquired at a reference time ($t = 0$) before any perturbation is made to the system. The resulting data residuals, $\delta_0 = \mathbf{d}_t - \mathbf{g}(\mathbf{b}_0) = \mathbf{e}_{\text{sys}} + \mathbf{e}_{\text{r},0}$, are removed from the data acquired at all subsequent times:

$$\tilde{\mathbf{d}}_t = \mathbf{d}_t - \delta_0 = \mathbf{g}(\mathbf{b}_t) + \mathbf{e}_{\text{r},t} - \mathbf{e}_{\text{r},0}. \quad (7)$$

The corrected data sets $\tilde{\mathbf{d}}_t$ used in the inversion at time-lapse t will be contaminated with less error provided that $\sigma_{\text{sys}} > \sqrt{\sigma_{\text{r},0}^2 + \sigma_{\text{r},t}^2}$, where σ_{sys} and σ_{r} are the standard deviations of the systematic and random errors, respectively.

2.3 Tracer plume parametrization

Our aim is to estimate the spatial distribution of the injected fluid in the subsurface. We describe this distribution in a uniformly discretized 3-D domain and present it in terms of the volume of fluid originating from injection over the volume of the voxel: θ_i [m^3/m^3], $i = 1, \dots, (nx \times ny \times nz)$, where x_i , y_i and z_i are the spatial coordinates and nx , ny and nz the number of voxels in the x -, y - and z -directions, respectively. Thus, θ_i is dimensionless and varies between 0 (no injected fluid) and a maximum value θ_{max} . Plumes that occupy large volumes will, for the same total injected volume, have smaller θ_{max} and vice versa, such that

$$\sum_{i=1}^{nx \times ny \times nz} \theta_i \Delta x \Delta y \Delta z = W^{\text{tot}}, \quad (8)$$

where Δx , Δy and Δz are the voxel dimensions and W^{tot} [m^3] is the total volume of fluid injected. The 3-D space described by θ is located in a sub-region of the MT forward mesh and is more finely discretized (see Fig. 1) to ensure the precision of the parametrization described in this section. We hereafter refer to this domain as the 'plume mesh'. A set of coordinates

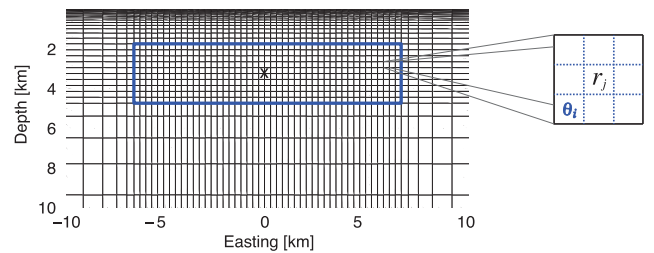


Figure 1. 3-D parameter discretization used in the inversions of the Paranal data set. The discretization along the north axis, not shown in the figure, is identical to the discretization along the east axis. The black lines represent the resistivity mesh (the complete extension to the sides and in depth is not shown), which is used as the MT forward mesh in the MCMC inversions and also as the inversion mesh in the deterministic inversions. The solid blue lines represent the limits of the subregion where the tracer plumes can be placed in the MCMC inversions. The dashed blue lines represent the discretization of the tracer plume as mapped from the Legendre parametrization (i.e. the plume mesh). The black cross indicates the injection point.

$\beta = (x_{\text{start}}, x_{\text{end}}, y_{\text{start}}, y_{\text{end}}, z_{\text{start}}, z_{\text{end}})$ describes the maximum extension of the subregion of the plume mesh where $\theta_i \neq 0$.

To reduce the number of parameters to invert for in the MCMC inversion, and to include W^{tot} as a fixed constraint on the proposed plume geometries, we use a model parametrization similar to the one proposed by Laloy *et al.* (2012). This parametrization is based on a reduced Legendre moment decomposition of the plume. The Legendre polynomials are orthogonal if defined in a unit square domain, and thus the Legendre moments are uncorrelated with each other (Teague 1980).

The Legendre moments λ of θ are given by

$$\lambda_{pqu} = \frac{(2p+1)(2q+1)(2u+1)}{8} \times \sum_{i=1}^{nx \times ny \times nz} P_p(x'_i) P_q(y'_i) P_u(z'_i) \theta_i \Delta x' \Delta y' \Delta z', \quad (9)$$

where x' , y' and z' are the transformed model coordinates on a unit square grid $[-1 \leq x', y', z' \leq 1]$, $\Delta x'$, $\Delta y'$ and $\Delta z'$ represent the voxel dimensions of the unit square, and $P_p(x'_i)$ is the Legendre polynomial of order p evaluated by numerical integration over cell i in the x -direction. In matrix notation, eq. (9) is described by

$$\lambda = \mathbf{P}\theta, \quad (10)$$

where \mathbf{P} contains the Legendre polynomial products on the 3-D unit grid. Then, θ can be reconstructed from its Legendre moments up to a given resolution defined by a truncated series expansion (Teague 1980),

$$\theta_i^{\text{rec}} = \sum_{p=0}^{O_{\text{max}}} \sum_{q=0}^{O_{\text{max}}} \sum_{u=0}^{O_{\text{max}}} \lambda_{pqu} P_p(x'_i) P_q(y'_i) P_u(z'_i), \quad (11)$$

where the superscript *rec* stands for ‘reconstructed’ and O_{max} is the maximum order of moments used for the reconstruction. Writing eq. (11) in matrix notation gives

$$\theta^{\text{rec}} = \mathbf{\Gamma}\lambda, \quad (12)$$

where $\mathbf{\Gamma}$ contains the polynomial product coefficients of the orthogonal moments and has dimension $(nx \times ny \times nz) \times n_{pqu}$, with $n_{pqu} = [(\max(p) + 1) \times (\max(q) + 1) \times (\max(u) + 1)]$.

The parametrization of θ in terms of the Legendre moments allows to propose plume models that satisfy certain desired constraints that increase the efficiency of the MCMC inversion. Here, the first imposed constraint concerns the total volume of injected water, which is directly related to the first Legendre moment:

$$\lambda_{000} = \frac{W^{\text{tot}}}{8} \frac{\Delta x' \Delta y' \Delta z'}{\Delta x \Delta y \Delta z}. \quad (13)$$

The remaining constraints force θ to be zero at the boundaries of the region defined by β . To implement these constraints, we follow Laloy *et al.* (2012) and construct a system of equations $\mathbf{A}\lambda = \mathbf{h}$ that contains all the constraints on λ , and calculate the singular value decomposition (SVD) of \mathbf{A}

$$\mathbf{A} = \mathbf{U}\mathbf{S}\mathbf{V}^T, \quad (14)$$

where \mathbf{U} and \mathbf{V} are orthogonal matrices that contain basis vectors spanning the space of constraints imposed in \mathbf{h} , and basis vectors spanning the model space for λ , respectively, and \mathbf{S} is a diagonal matrix with the singular values sorted in decreasing order.

According to Laloy *et al.* (2012), \mathbf{S} will typically have k significant singular values related to the preservation of injected water volume and zero-constraints for θ on the boundaries given by β .

Then, the solutions to the inverse problem will have the general form

$$\lambda = \mathbf{V}_k \mathbf{S}_k^{-1} \mathbf{U}_k^T \mathbf{h} + \mathbf{V}_0 \alpha, \quad (15)$$

where \mathbf{V}_k , \mathbf{S}_k and \mathbf{U}_k have dimensions $n_{pqu} \times k$, $k \times k$ and $N_{\text{prior}} \times k$, respectively. The first term on the right side of eq. (15) ensures that λ satisfies the desired constraints and we thus keep these values fixed. Conversely, the second term, specifically the vector α , can take any value while still creating models that honour the constraints. We invert for α in the MCMC inversion scheme such that the inferred models honour the data.

The constraints described above do not prevent the generation of models containing negative values (i.e., $\theta_i < 0$). To avoid such models we set to zero the negative values and then pre-multiply each θ_i by a factor of $W^{\text{tot}}/W^{\text{tot}'}$, where $W^{\text{tot}'}$ is the total fluid volume without considering the negative values. By doing so, the new plumes conserve the injected water volume.

We evaluate the basic geometrical properties of the resulting plumes in terms of their centre of mass:

$$\begin{cases} \mu_{xc} = \frac{1}{W^{\text{tot}}} \sum_{i=1}^{nx \times ny \times nz} \theta_i x_i \Delta x' \Delta y' \Delta z', \\ \mu_{yc} = \frac{1}{W^{\text{tot}}} \sum_{i=1}^{nx \times ny \times nz} \theta_i y_i \Delta x' \Delta y' \Delta z', \\ \mu_{zc} = \frac{1}{W^{\text{tot}}} \sum_{i=1}^{nx \times ny \times nz} \theta_i z_i \Delta x' \Delta y' \Delta z', \end{cases} \quad (16)$$

and spread:

$$\begin{cases} S_{xx} = \sqrt{\frac{1}{W^{\text{tot}}} \left(\sum_{i=1}^{nx \times ny \times nz} \theta_i x_i^2 \Delta x' \Delta y' \Delta z' \right) - \mu_{xc}^2}, \\ S_{yy} = \sqrt{\frac{1}{W^{\text{tot}}} \left(\sum_{i=1}^{nx \times ny \times nz} \theta_i y_i^2 \Delta x' \Delta y' \Delta z' \right) - \mu_{yc}^2}, \\ S_{zz} = \sqrt{\frac{1}{W^{\text{tot}}} \left(\sum_{i=1}^{nx \times ny \times nz} \theta_i z_i^2 \Delta x' \Delta y' \Delta z' \right) - \mu_{zc}^2}. \end{cases} \quad (17)$$

2.4 Petrophysics and upscaling procedure

In this subsection, we explain how we translate θ into corresponding bulk resistivity values, from which the MT response can be evaluated. Let the base model, that is, the 3-D resistivity distribution prior to the injection be described by a vector $r_{j,0}$, $j = 1, \dots, (NX \times NY \times NZ)$, with NX , NY and NZ the number of resistivity blocks in the x -, y - and z -direction, respectively. The black mesh in Fig. 1 represents this discretization. We assume that the region where fluid is injected is saturated with water of constant resistivity. Taking $\Phi_{j,t}$ to be the porosity at the scale of the resistivity discretization, and using Archie’s law (Archie 1942) gives

$$r_{j,0} = \rho_w^{\text{pre}} \Phi_{j,0}^{-m_0}, \quad (18)$$

where m_0 is the cementation factor prior to the injection, which we assume to be known, and ρ_w^{pre} is the resistivity of the pre-existing fluid at the confining rock temperature. We assume that the conductive fluid dominates the conduction in the fracture network (e.g. Brace *et al.* 1965), and surface conductivity is thus neglected.

The fluid resistivity is a function of temperature and salt concentration. We use the relationship by Sen & Goode (1992) to model this dependence:

$$\rho_w(T, c) = \left[(5.6 + 0.27T - 1.5 \times 10^{-4} T^2) c - \frac{2.36 + 0.099T}{1 + 0.214c} c^{3/2} \right]^{-1} \Omega\text{m}, \quad (19)$$

where c is the salt concentration in mol l^{-1} and T the temperature in $^\circ\text{C}$. Given a proposed spatial distribution of the tracer plume at time

$t, \theta_{i,t} [\text{m}^3/\text{m}^3]$, we consider the possibility of an increase in porosity due to the opening of fractures, $\Delta\phi_{i,t}$, where $\phi_{i,t}$ represents the porosity. The bounds for the porosity change are given by $0 \leq \Delta\phi_{i,t} \leq \theta_{i,t}$. To obtain the salt concentration of the fluid at time t in each model block, we sum the contributions from the salt concentration of the injected water and the salt concentration of the water prior to the injection, weighted by the volume they occupy in the available space:

$$c_{i,t} = \frac{\theta_{i,t}}{\phi_{i,t}} c^{\text{inj}} + \frac{\phi_{i,t} - \theta_{i,t}}{\phi_{i,t}} c^{\text{pre}}, \quad (20)$$

where $\phi_{i,t} = \phi_{i,0} + \Delta\phi_{i,t}$.

If new fractures are opened it is likely that the cementation factor decreases (e.g. Jougnot & Revil 2010). As a first approximation, we model the changes of the cementation factor $\Delta m_{i,t}$ to be proportional to $\theta_{i,t}$

$$\Delta m_{i,t} = \frac{\theta_{i,t}}{\theta_{t,\text{max}}} \Delta m^{\text{max}}, \quad (21)$$

where the maximum change in the cementation factor Δm^{max} is one of the parameters to be estimated within the inversion. The cementation factor at time t will then be given by $m_{i,t} = m_0 + \Delta m_{i,t}$.

To reduce the computation time of the forward responses, it is important to make the MT forward mesh as coarse as possible. At the same time, the plume mesh should be fine enough to ensure the precision of the Legendre moment decomposition. Here, we propose to upscale the finely discretized plume description and then use Archie's law to calculate the corresponding resistivity distribution

of the MT forward mesh (Fig. 1). We volume-average the porosity and the cementation factor within each MT forward block:

$$\begin{cases} \Phi_{j,t} = \sum_{i \in V_j} \frac{\phi_{i,t} V_i}{V_j}, \\ M_{j,t} = \sum_{i \in V_j} \frac{m_{i,t} V_i}{V_j}, \end{cases} \quad (22)$$

where V_i and V_j are the volumes of the fine plume mesh and MT forward mesh blocks, respectively. Correspondingly, the total amount of salt in each of the coarse blocks is given by:

$$S_{j,t} = \sum_{i \in V_j} c_{i,t} \phi_{i,t} V_i. \quad (23)$$

We use this value to calculate the upscaled fluid salt concentration $C_{j,t} = \frac{S_{j,t}}{\Phi_{j,t} V_j}$, which in turn is used in eq. (19) to calculate an up-scaled fluid resistivity. Finally, the coarse-mesh bulk resistivity at time t , $r_{j,t}$, is calculated using eq. (18) with the upscaled porosity, cementation factor and fluid resistivity.

The posterior pdf that we seek to sample with MCMC simulations is given by

$$p(\mathbf{b}_t | \tilde{\mathbf{d}}_t) \propto p(\mathbf{b}_t) L(\mathbf{b}_t), \quad (24)$$

where $\mathbf{b}_t = [\alpha, \beta, \Delta m^{\text{max}}]$. Fig. 2 summarizes our probabilistic inversion methodology and the upscaling procedure.

2.5 Resistivity-difference-based probabilistic time-lapse inversion

In cases where the petrophysical relations described above do not apply, or the information about the time-lapse experiment is limited, the classical approach is to infer the resistivity contrasts needed to explain the data changes (e.g. Falgàs *et al.* 2009). Here, we present such an approach while conserving the Legendre moments

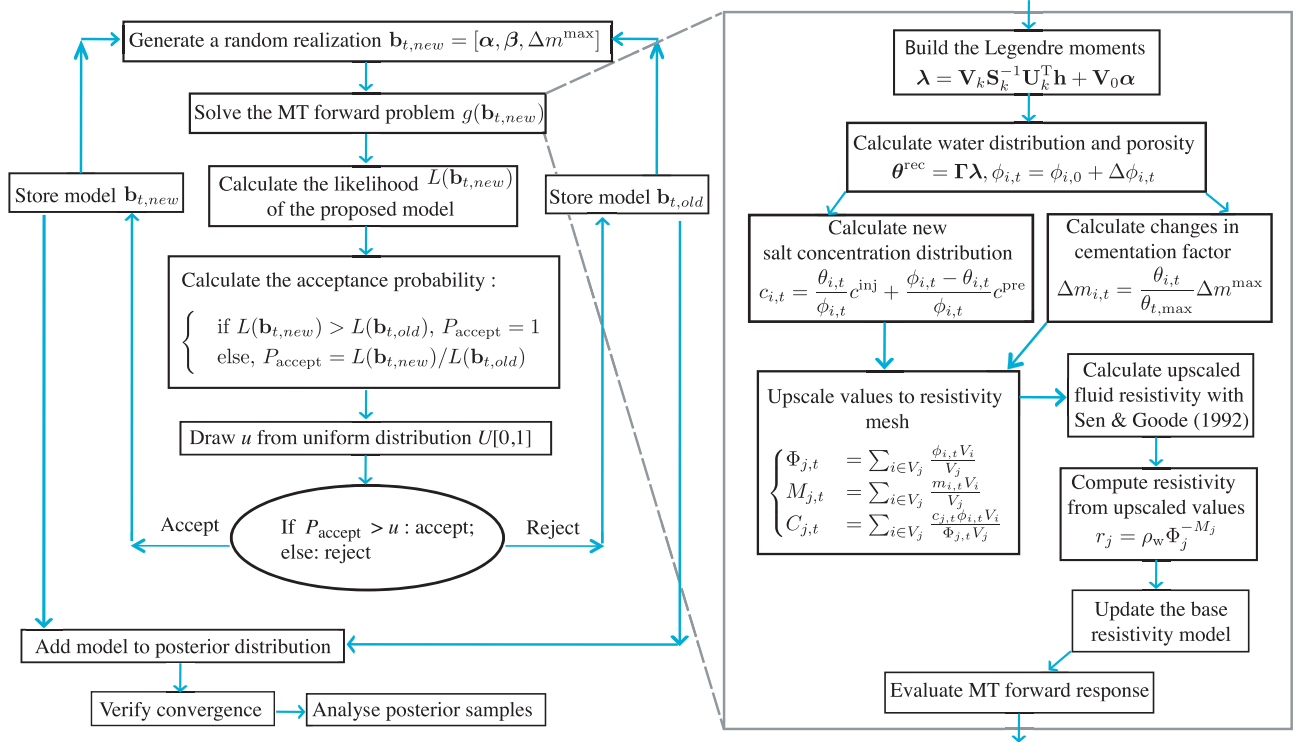


Figure 2. Schematic overview of the MCMC inversion framework used to invert the time-lapse MT data. The left side describes the MCMC algorithm applied to one of the parallel chains used in DREAM_(ZS). The right side highlights the upscaling procedure used to transform the proposed tracer plume model to a resistivity model that can be used to evaluate the corresponding MT response.

parametrization to reduce the number of parameters. We propose the following relation between the resistivity ratio and the spatial variations given by the Legendre moments

$$\frac{r_{1,j}}{r_{0,j}} = \begin{cases} 1, & \text{if } \Theta_j = 0, \\ 10^f \Phi_0^{\frac{\Theta_j}{\Theta_{\max}}}, & \text{otherwise,} \end{cases} \quad (25)$$

where f is a parameter to be inferred in the inversion, Θ the upscaled θ and Θ_{\max} its maximum value. Taking the logarithm of eq. (25) to consider the resistivity changes $\Delta \log_{10} \mathbf{r} = \log_{10}(\mathbf{r}_1/\mathbf{r}_0)$, it can be noted that f acts as a shift on the spatial variations imposed by $\frac{\Theta_j}{\Theta_{\max}}(\log_{10} \Phi_0)$. For a given Θ and negative f , the maximum change in resistivity with respect to the base model is given by $\Delta \log_{10} r_{\max} = f + \log_{10} \Phi_0$.

2.6 3-D deterministic inversion

To obtain the base resistivity model needed for the time-lapse inversions, we resort to classical deterministic inversion. To the best of our knowledge, no attempts have been made so far to use MT data to obtain the posterior pdf of a 3-D resistivity model discretized in voxels. This is because the large number of unknowns would imply a large number of iterations to converge to the posterior distribution (*cf.* Rosas-Carbajal *et al.* 2014), and the forward solvers still require significant CPU time to calculate the 3-D forward model response. We use the ModEM program (Egbert & Kelbert 2012) with non-linear conjugate gradients (*e.g.* Nocedal & Wright 2006) to perform the deterministic inversions.

3 THE PARALANA TEST SITE

The Paralana geothermal system is located in Paralana, South Australia. Its anomalously high heat flow, estimated at 113 mW m^{-2} (Neumann *et al.* 2000), is associated with an unusual concentration of radiogenic elements within the Mount Painter Domain (Brugger *et al.* 2005). This domain is composed of fractured Paleoproterozoic to Mesoproterozoic gneiss, granites and metasediments. Well testing and fracture stimulation were carried out in view of developing a power supply from the geothermal sources. In 2009, an injection well was drilled to 4000 m depth and cased to 3725 m. Several zones of over-pressured fluid were encountered between 3670 and 3864 m (Reid *et al.* 2011) and the measured temperature at the bottom of the borehole was 190°C . Saline fluids with a resistivity of $1.5 \Omega\text{m}$ (at ambient temperature) were encountered at 3860 m, indicating a pre-existing fluid-filled fracture network (Peacock *et al.* 2013).

In July 2011, 3100 m^3 of saline water of resistivity $0.3 \Omega\text{m}$, along with acids, were injected into the metasediments to stimulate the opening of new fractures. The injection was carried out at a depth of 3680 m over the course of 4 d. During the injection, a microseismic array measured over 11 000 events with the majority located in the northeast quadrant from the injection well (Hasting *et al.* 2011). The data suggest that fractures opened in a preferred northeast direction and that the total zone stimulated by the injection was approximately 900 m in the northeast–southwest direction, over a depth extent of 600 m. After the injection, the wellhead pressure remained at approximately 27.6 MPa, suggesting that the stimulated volume is connected to a naturally over-pressured zone (Reid *et al.* 2011).

Peacock *et al.* (2012) presented the results of the continuous monitoring of the 4-d injection with 11 MT stations placed around the borehole. Peacock *et al.* (2013) reported on time-lapse measurements of about 50 MT stations acquired just before and 1 week

after the injection experiment. They observed coherent changes in the MT signals above measurement errors, indicating predominant resistivity changes in the north–northeast direction. In the following section, we use these data in an attempt to infer the spatial distribution of the injected tracer 1 week after the injection was finalized. We refer to Peacock *et al.* (2012) and Peacock *et al.* (2013) for details about the MT transfer function estimation.

4 RESULTS

4.1 Base resistivity model from 3-D deterministic inversion

To evaluate the changes in resistivity produced by the injected water, a base model representing the subsurface resistivity prior to the injection is needed (Rosas Carbajal *et al.* 2012). Fig. 3 depicts the location of the 60 MT stations used to obtain this model. Besides the time-lapse stations (*i.e.*, those repeated post-injection), additional stations were used to obtain the base model.

We first perform 1-D MCMC inversions to obtain layered models that are parametrized in terms of the logarithms of resistivity and layer thickness, for 2, 3, 4 and 5 layers. The 1-D forward solver is described by Linde & Pedersen (2004). We use the off-diagonal components of the impedance tensor of 60 stations with 12 periods ranging from 0.016 to 161 s and assume an error floor of 5 per cent on the impedance elements. The results of these inversions will subsequently be used as starting models of deterministic 3-D inversions. Since the latter are limited to the use of an l_2 -norm to measure the data misfit, we also use an l_2 -norm for the data misfit in the 1-D MCMC inversions. The prior pdf consists of uniform distributions in the range of -2 to 4 for \log_{10} -resistivity, and 1 to 4 for \log_{10} -thickness. Fig. 4(a) shows some posterior realizations of these inversions, and Figs 4(b) and (c) display the forward response of the posterior mean models compared to the measured apparent resistivity and phase, respectively. The uncertainty in the posterior pdf increases with the degrees of freedom, and thus, the number of layers. The improvement in data fit from the mean model with 4 layers to the mean model with 5 layers is subtle (RMS of 6.77 and 6.6, respectively). Furthermore, the inversion considering five layers proposes a very thin and conductive layer (located at about 10 km depth), which appears unphysical. The data presented in Figs 4(b) and (c) shows evidence of heterogeneity or anisotropy that cannot be explained with 1-D isotropic models. Therefore, we use the mean model from the posterior pdf with 4 layers as the starting

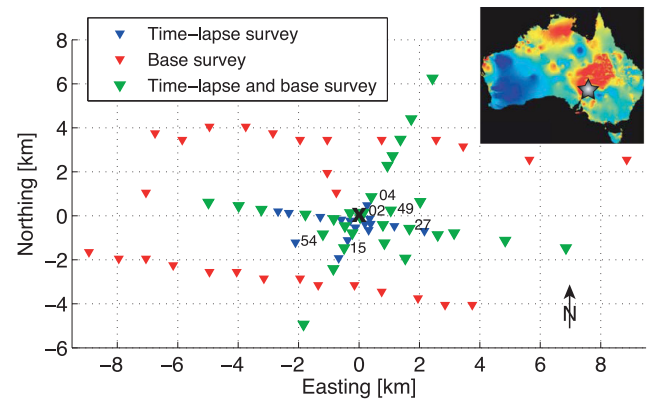


Figure 3. Magnetotelluric stations used for the base and time-lapse inversions in Paralana, represented in a local grid with the injection point in the centre (x). At the top right corner, a map of Australia shows the temperature at 5 km depth where red represents 285°C and the star locates Paralana.

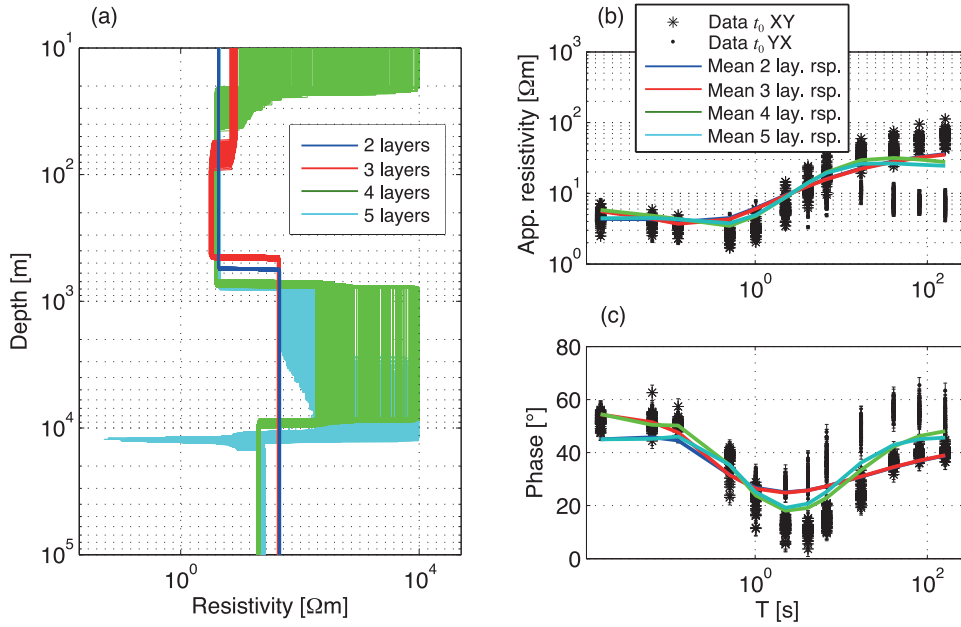


Figure 4. (a) Posterior realizations of the 1-D MCMC inversions of the base data using different (fixed *a priori*) number of layers. Corresponding data in terms of (b) apparent resistivities and (c) phases are shown together with the simulated responses of the posterior mean models, where the *X*-direction corresponds to the north and the *Y*-direction to the east. The model with 4 layers represents a compromise between low data misfit and few model parameters. The forward responses of the 1-D models explain the general tendency of the data at low periods but cannot describe the separation between the *XY* and *YX* data at higher periods.

model of the 3-D deterministic inversion. The layer thicknesses and resistivities in this model from surface to depth are given by

$$\begin{cases} h_1 = 33 \text{ m}, & r_1 = 70 \text{ } \Omega\text{m}, \\ h_2 = 700 \text{ m}, & r_2 = 4 \text{ } \Omega\text{m}, \\ h_3 = 7780 \text{ m}, & r_3 = 550 \text{ } \Omega\text{m}, \\ h_4 = \text{half-space}, & r_4 = 20 \text{ } \Omega\text{m}. \end{cases} \quad (26)$$

We use the ModEM program (Egbert & Kelbert 2012) to perform the deterministic 3-D inversion. Since the diagonal components of the impedance tensor are strongly noise contaminated, we do not use them in any of the inversions. Thus, we invert the same data as for the 1-D MCMC inversion, and we obtain a final RMS of 1.35 after 99 iterations.

Fig. 5(a) shows vertical slices of the inverted 3-D model at the centre of the *x*- and *y*- axes and for horizontal slices at 700 m and 3700 m (injection) depth. Most of the variability with respect to the starting model is present at shallow depths whereas only minor changes are introduced at the injection depth. According to this model, the injection takes place in a thick resistive layer. We present the comparison between the model response and the data for some stations in Fig. 5(b). Both apparent resistivity and phase curves are clearly better explained by the 3-D model than by the 1-D model (see Figs 4b and c).

4.2 Time-lapse 3-D deterministic inversion

Fig. 6 illustrates some of the changes observed with respect to the base data one week after the injection (defective stations were removed). Initial inversions using both apparent resistivity and phases lead to very erratic resistivity changes, which may be due to different galvanic distortions affecting the base and time-lapse data. Hence, we decided to only use the phase data for the deterministic and probabilistic time-lapse inversions.

Following the differencing strategy presented in Section 2.2, we compute the data residuals from the base model and remove them from the post-injection data. Not all the stations could be repeated using the same holes for installing the MT stations, however, we applied the time-lapse strategy to all the stations assuming that in cases where the station locations were not exactly the same this would still remove most of the systematic modelling errors. To describe the resulting errors, we use the combination ($\sigma_{r,\text{tot}} = \sqrt{\sigma_{r,0}^2 + \sigma_{r,t}^2}$) of the errors pre- and post-injection provided by the impedance transfer function estimations. In addition, we use an error floor of 1° to ensure that data are not over-fitted. Finally, we remove 6 data points corresponding to the longer periods at 3 different stations because they present extremely large estimated errors. This results in a total of 676 data points.

Using the 3-D base model (Fig. 5a) as the starting model, we perform a deterministic time-lapse inversion of the data. The RMS of the starting model is 2.8 and the final RMS is 1.01, which corresponds to a data misfit of $\varphi_{l_2} = 690$. Depth slices of resistivity changes at 700 and 3700 m depth are presented in Figs 7(a) and (b). As expected, most changes indicate a decrease in the electrical resistivity. The resistivity decrease at the injection depth (Fig. 7b) is elongated in the north–south direction and is of much smaller magnitude than at 700 m depth (resistivity contrasts with respect to the base model are approximately two orders of magnitude smaller). The adequate data misfit and the agreement between the data and the forward responses in Fig. 7(c) suggest that this model explains most of the time-lapse data.

4.3 Synthetic time-lapse MCMC inversion

To evaluate our probabilistic 3-D time-lapse inversion strategy, we first consider a synthetic test case. The example is similar to the

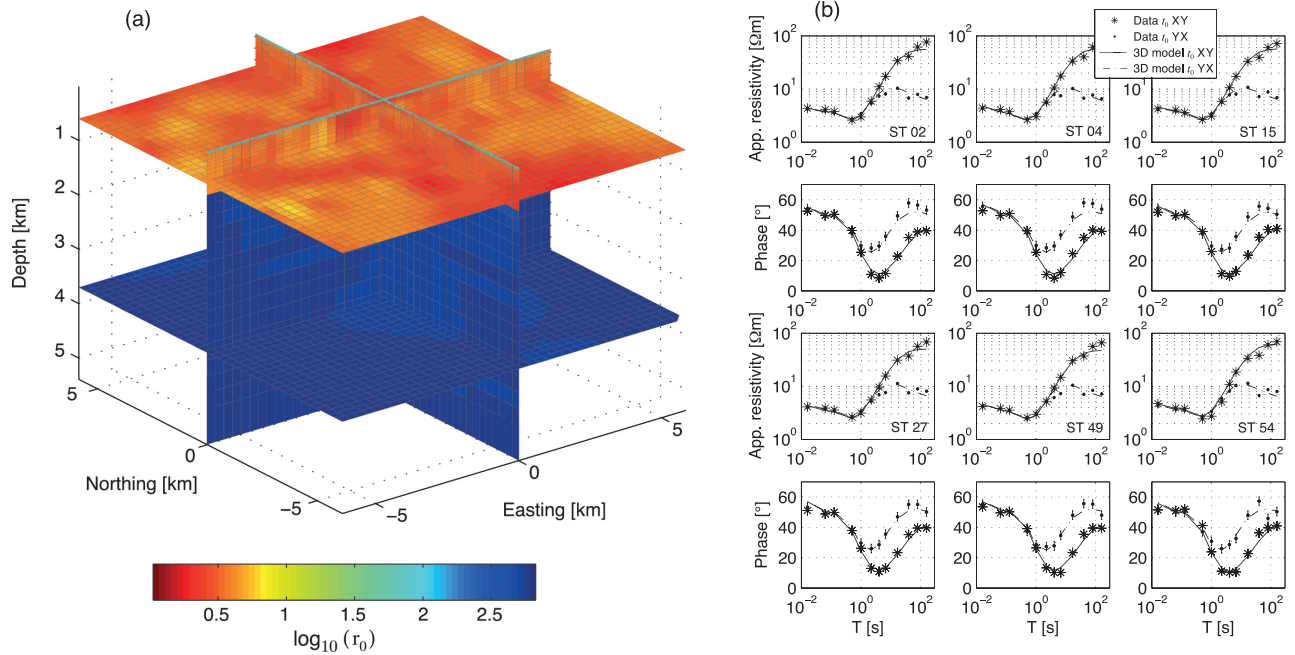


Figure 5. (a) 3-D base model at Paralana obtained from the deterministic inversion of the base data using ModEM (Egbert & Kelbert 2012) and the mean 1-D model with 4 layers from Fig. 4 as the starting model. Horizontal depth slices correspond to 700 and 3700 m (injection) depth. (b) Base data and forward response of the model shown in (a) for some of the MT stations (see locations in Fig. 3).

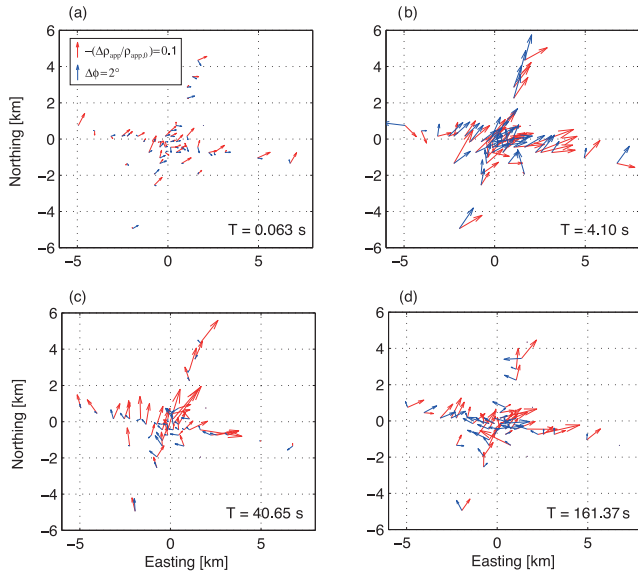


Figure 6. Relative apparent resistivity and absolute phase changes observed in the data one week after the injection as a function of station position, for some of the periods considered. Changes are represented by arrows, where the length is proportional to the l_2 -norm of the off-diagonal impedance changes and the orientation depicts the relative weight between changes in the XY and YX components. A vertical arrow indicates changes in the XY component only. Phase changes are largest at $T = 4.10$ s (panel b). This figure is shown as a station-to-station comparison only. For phase tensor representation, see Peacock *et al.* (2013).

real experiment in that we assume being in possession of the same amount and type of information in terms of the station distribution, periods and data errors. In addition, we assume that the base model previously obtained (Fig. 5a) is the real one, and insert in

this model a 3-D plume calculated with a Legendre moment decomposition of order 3. For this, we use the same temperature and salinity constraints as the ones from the real experiment, but we assume that the mass injected is six orders of magnitude larger than in the real case, and that the injection is done at a depth of 2700 m, that is, 1 km more shallow than the real experiment. These drastic changes compared to the field experiment were needed to reproduce the observed magnitudes of the time-lapse data at Paralana. Finally, we assign a maximum change in the cementation factor of $\Delta m^{\max} = -0.5$.

To generate the synthetic plume we use the scheme shown on the right side of Fig. 2. We consider the porosity presented in eq. (18) to be the crack porosity, that is, the ratio between the volume of open fractures in the rock and the total rock volume. This value is calculated using eq. (18) with the base resistivity model and assuming $m = 2$ over the complete domain. The fluid resistivity at the borehole temperature is calculated using eq. (19) with the values obtained from fluid samples and temperature measured at the injection borehole. Eq. (18) gives, for an average resistivity value of 550 Ωm at the injection depth, an average crack porosity of 2.5 per cent. We further assume that the space created by the rock dissolution and opening of fractures in each voxel is equal to the volume of fluid that originates from the injection in that voxel, that is, $\Delta\phi_{i,t} = \theta_{i,t}$. This implies that the volume of pre-existing fluids does not change since the extra volume needed for the injected fluids is given by the porosity increase. This simplification maximizes the predicted resistivity changes. We adopt the same assumption in the inversion of the field data. Fig. 8(a) shows the selected geometry of the synthetic plume represented as the volume of subsurface where salinity has changed. The plume is predominantly oriented in the north–south direction and presents a bend towards the east in the northern extreme. In depth, it extends from ~ 1.5 to ~ 3.3 km. The northeast extreme of the plume has smaller tracer water content than the north–south portion. The centre of mass and spread are

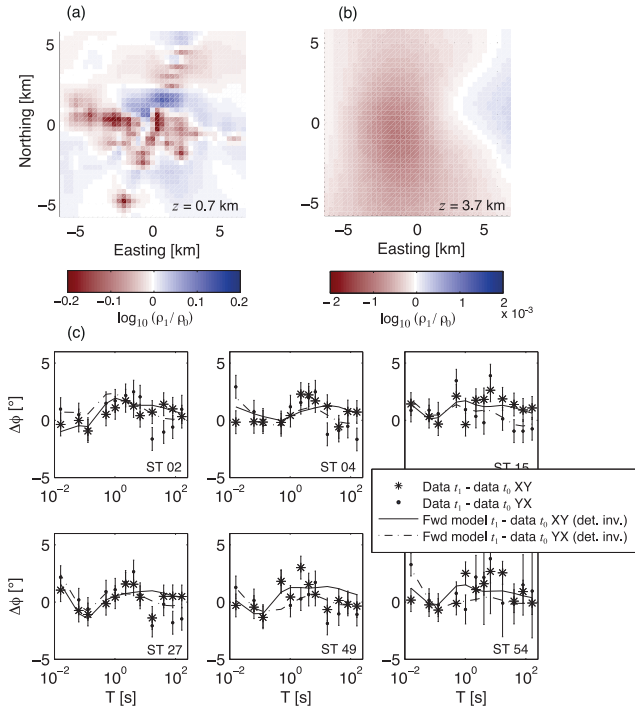


Figure 7. (a,b) Estimated differences in log-resistivity after the injection with respect to the base model (Fig. 5a), obtained with a deterministic 3-D time-lapse inversion. The depth slices correspond to (a) 700 m and (b) 3700 m (injection depth). (c) Post-injection differences of data and forward response of the model shown in (a) and (b) for some of the stations measured, with respect to the data shown in Fig. 5(b) (see station locations in Fig. 3). The resistivity changes are concentrated at shallower depths than the injection point. The model explains the time-lapse data (RMS = 1.01), but note also the low signal-to-noise-ratios in this field example.

given in Table 1. The spread in the north–south direction is ~ 900 m larger than in the east–west direction.

Fig. 8(b) shows the corresponding resistivity changes with respect to the base model calculated as described in Section 2.4 and Fig. 2. Maximum resistivity changes of two orders of magnitude are found close to the injection point ($x = y = 0$ in Fig. 8b). In the northeastern part, the resistivity changes are ~ 1 order of magnitude. To simulate the synthetic data, we contaminate the forward response of this new resistivity model with errors following an exponential distribution with a mean deviation (see eq. 5) equal to the standard deviation used for the deterministic inversion. We use this distribution to obtain similar errors to the ones observed in the Paralana data. The resulting synthetic data, shown for some stations in Fig. 8(c), have deviations from the base model response that are similar to the field data (cf. Fig. 7c).

The model parametrization used for the synthetic and field-based inversions is based on a Legendre decomposition up to order 3 (see Section 2.3). This means that, besides the 6 coordinate parameters in β and the maximum change in the cementation factor Δm^{\max} , 7 coefficients α_i , $i = 1, \dots, 7$ need to be determined by the inversion, thus yielding a total of 14 model parameters to invert for. Following Laloy *et al.* (2012), we assign uniform prior distributions for these coefficients in the range $[-0.1, 0.1]$, which contain the values used to create the synthetic plume. For the coordinates of the plume boundaries, we determine a maximum extension of 13.8 km in the east–west and north–south directions and of 3.3 km in depth. Then, we discretize this volume in cubes of $75 \times 75 \times 75$ m³ to obtain the injected water distribution θ from the Legendre moments. Thus,

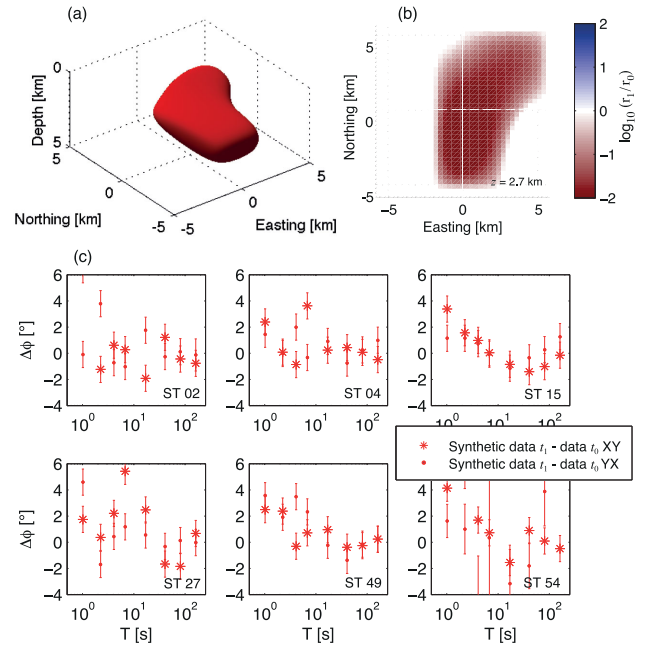


Figure 8. Synthetic plume used to test the MCMC inversions based on the Legendre moment decomposition. (a) Plume geometry at the fine discretization used for the Legendre decomposition. The isovolume corresponds to a value of $\theta = 10^{-7}$. (b) Differences in log-resistivity with respect to the base model (Fig. 5a) at the injection depth of 2700 m. (c) Time-lapse data simulated from the synthetic model and contaminated with noise corresponding to the same errors as assumed for the field data. The plume has a predominant north–south direction with a bend towards the northeast at its northern side.

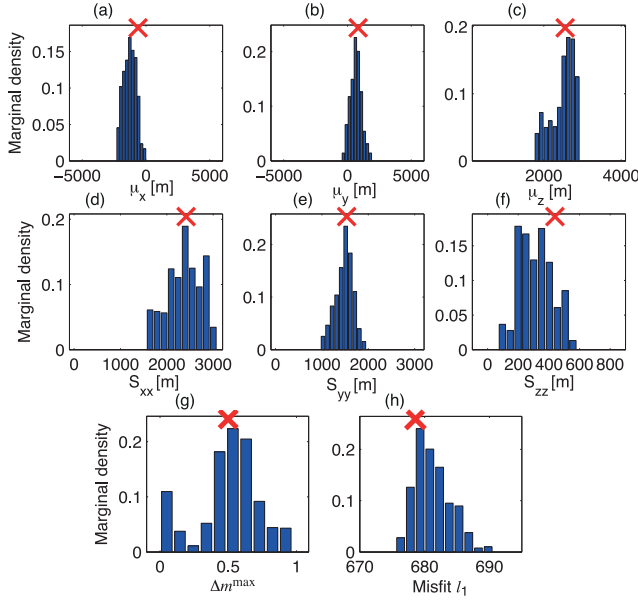
x_{start} and y_{start} can take discrete (every 75 m) values between -6.9 km and 0 km; x_{end} and y_{end} can take values between 0 and 6.9 km; and z_{start} and z_{end} can vary between 0.5 and 2.15 km, and 2.15 km and 3.8 km, respectively. To translate the plume to a resistivity model, we discretize the same volume in cubes of $300 \times 300 \times 300$ m³. This discretization was chosen based on a convergence test of the mesh, in which we evaluated the forward response (also calculated with ModEM) of the base model containing a conductor of the size of the maximum plume allowed for different lengths of the domain and resistivity block sizes. The chosen resistivity discretization represents a compromise between accurate forward responses, that is, changes in impedance of less than 0.1 per cent with respect to a highly discretized and largely extended mesh, and computation time.

We allow Δm^{\max} to vary between 0 , that is, no change in the cementation factor, and -0.99 , which implies $m^{\min} \approx 1$ and thus a perfectly connected medium. We use uniform prior distributions for all the model parameters mentioned, and an l_1 -norm in the likelihood function to evaluate the data misfit (see eq. 5) since the errors follow an exponential distribution.

We use the DREAM_(ZS) algorithm with three chains that evaluate the forward responses in parallel. We also employ the parallelized forward solver in ModEM, which distributes the forward computations for each period and for each of the two EM field polarizations to a different processor. To decrease the number of processors needed, we only use the 8 longest periods in the MCMC inversions, which is where the main time-lapse changes occur. Since we evaluate eight periods for each configuration, we use 16 processors per chain, and thus a total of 48 processors for the forward computations. The computing time of a single forward response depends on the

Table 1. Mean values and standard deviations of the centre of mass and spread of the synthetic plume, as estimated with the probabilistic mass-constrained time-lapse approach.

Model	Estimate	Centre of mass			Spread			Δm^{\max} [–]	Data misfit [–]
		μ_{xc} (m)	μ_{yc} (m)	μ_{zc} (m)	S_{xx} (m)	S_{yy} (m)	S_{zz} (m)		
True	N/A	–620	840	2550	2420	1530	440	–0.5	676
Order 3	Mean	–1160	670	2490	2370	1480	370	–0.48	682
	Standard deviation	490	440	310	370	190	110	0.24	3

**Figure 9.** (a–f) Marginal posterior distributions of the centre of mass (a–c) and spread (d–f) of the plume for the synthetic test. The ranges of values shown correspond to the prior pdfs’ bounds. (g) Maximum change of the cementation factor. (h) Data misfit distribution of the posterior models’ responses to compare with the 676 data points used. The red crosses indicate the true values. The histograms’ mean and standard deviation are indicated in Table 1.

complexity of the model evaluated, but is on average 11 min. Convergence of the chains was reached after ~ 7500 realizations, which, multiplying by the number of chains implies a total of $\sim 22\,500$ forward computations. The mean acceptance rate was 40 per cent and the total computing time needed to reach convergence was approximately 60 d.

Figs 9(a)–(f) show the marginal posterior distributions of the plume’s centre of mass and spread, and Δm^{\max} . All the parameter values used to construct the synthetic plume are contained in the posterior pdf. Fig. 9(h) shows the data misfit distribution of the models that belong to the posterior pdf. The corresponding model responses have data misfits that are close to the true value (676). Table 1 shows the mean and standard deviation of the histograms shown in Fig. 9. The centre of mass estimate in depth is very well determined, being only 60 m more shallow than the true value, while in the x -direction, it is approximately 450 m to the south from the exact value. The standard deviations of the centre of mass estimates are in the order of 400 m. The spreads of the plume are well determined, with a larger uncertainty in the x -direction. The cementation factor change of -0.5 is well estimated with a mean value of -0.48 and a standard deviation of 0.24 . The posterior data misfit distribution is short-tailed and close to the number of data.

In Figs 10(a)–(f), we present some of the plumes that belong to the posterior distribution. In agreement with the true model, the plumes are mostly located in the eastern part of the region and are elongated in the north–south direction. Only two plumes (Figs 10b and e) present a larger extension to the northeast similar to the true plume.

4.4 Application to the Paralana injection experiment

We now return to the field data acquired during the injection experiment in Paralana. We first perform a MCMC inversion with the same model parameters as for the synthetic case and the same prior distributions, but with the actual water volume. Also, the discretization in cubes of $300 \times 300 \times 300$ m³ is shifted downwards 1.1 km in z to allow for deeper plumes. Thus, z_{start} and z_{end} can vary between 1.6 and 3.25 km, and 3.25 and 4.9 km, respectively.

The base model l_1 -norm data misfit of the time-lapse data is $\varphi_{l_1} \approx 1980$ and the MCMC inversion reaches a data misfit that oscillates around $\varphi_{l_1} \approx 750$ for our 676 data (i.e., the data are not fitted to the error model). The spread estimates shown in Table 2, $S_{xx} = 2820$ m, $S_{yy} = 2900$ m, $S_{zz} = 710$ m, have a tendency to maximize the size of the plume (the prior ranges of β result in allowed maximum spreads of 3100 m in the horizontal directions and 740 m in depth). Moreover, Δm^{\max} , which largely controls the changes in the resistivity with respect to the base model, is close to the maximum value allowed, that is, -0.99 . This behaviour of the spread and Δm^{\max} indicates that resistivity changes larger than allowed by our physical model are needed to explain the time-lapse changes.

To investigate the actual resistivity changes needed to explain the data, we resort to the resistivity-difference-based time-lapse inversion presented in Section 2.5. We use the same Legendre moment decomposition up to order 3 as in the previous inversions, with the same prior ranges for α and β , and a uniform prior pdf between -10 and 0 for f . The MCMC inversion converged after $\sim 13\,500$ realizations (40 500 forward computations), with a mean acceptance rate of 25 per cent and 95 d of total computation time. Fig. 11 shows the posterior estimates of the mean and standard deviation of the centre of mass, spread and the maximum resistivity change Δr_{\max} and data misfit. The posterior uncertainty ranges of the spreads are no longer affected by the prior boundaries (see Table 2). The centre of mass of the plume is located towards the south of the injection point and it is well centred in the east–west direction. The centre of mass is estimated at a depth that is ~ 150 m deeper than the actual injection point, with a standard deviation of 130 m. In accordance with the microseismics (Reid *et al.* 2011), the spread is larger in the north–south direction than in the east–west direction. The posterior pdf of $\Delta \log_{10} r_{\max}$ has a mean value of -7.3 with a standard deviation of 0.3 . The posterior models have data misfit values that are smaller than the number of data with the data misfit distribution centred on 575.

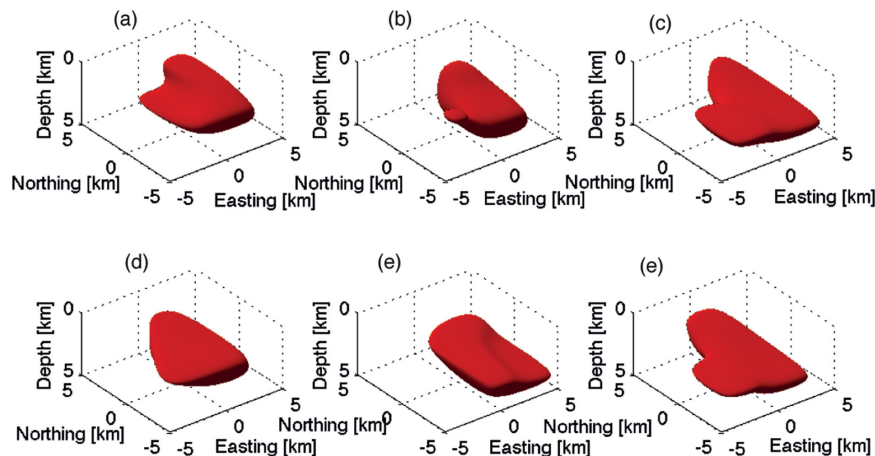


Figure 10. (a–f) Random posterior realizations from the MCMC inversion of the synthetic time-lapse data. Models have a predominant north–south direction and similar extension to the true plume (Fig. 8a). The isosurfaces correspond to a value of $\theta = 10^{-7}$.

Table 2. Mean and standard deviation of the estimated centre of mass and spread of the injected plume at Paralana, as estimated with the mass-constrained and resistivity-difference-based probabilistic time-lapse inversion approaches.

Type of inversion	Estimate	Centre of mass			Spread			Δm^{\max} [–]	$\Delta \log_{10} r^{\max}$ [–]	Data misfit [–]
		μ_{xc} (m)	μ_{yc} (m)	μ_{zc} (m)	S_{xx} (m)	S_{yy} (m)	S_{zz} (m)			
Petrophysically based	Mean	–460	1010	2830	2820	2900	710	–0.95	N/A	750
	Standard deviation	390	1070	110	210	100	60	0.04	N/A	7
Resistivity-difference based	Mean	–2540	10	3830	2260	1630	530	N/A	–7.3	574
	Standard deviation	440	550	130	180	160	60	N/A	0.3	9

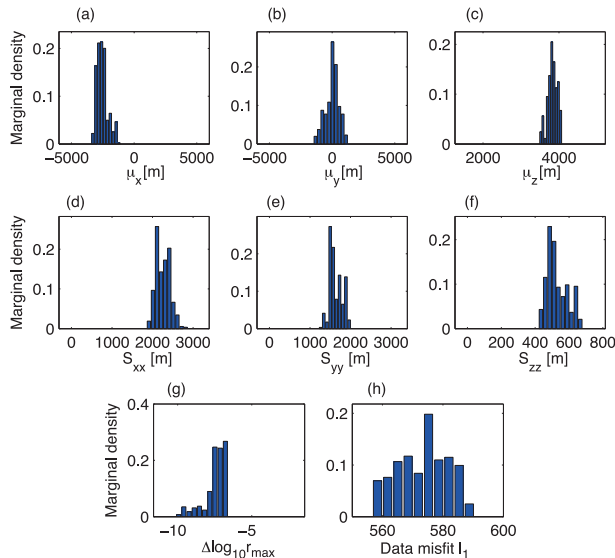


Figure 11. (a–f) Marginal posterior distributions of the centre of mass (a–c) and spread (d–f) of the plume from the resistivity-difference-based Paralana time-lapse inversion. The range of values shown corresponds to the prior pdfs' bounds. (g) Maximum resistivity change. (h) Data misfit distribution of the posterior models to compare with the 676 data points used. The histograms mean and standard deviation are indicated in Table 2.

The posterior models shown in Figs 12(a)–(f) indicate that the plume is most likely oriented in a north–south direction, and rather to the east. In depth, most models extend between 3400 m and 4500 m but with depth variations along the plume. Some models

(Figs 12b, c, d and f) show a plume dipping towards the north, as suggested by the microseismic data by Reid *et al.* (2011). An isolated component of the plume can be observed in Figs 12(b), (d) and (f) in the northeast region at more shallow depths (~ 3400 m) than the rest of the plume.

5 INFLUENCE OF THE BASE MODEL

The previous results suggest that large resistivity changes are needed to explain the Paralana time-lapse data. These changes are presumably dependent on the base model from which they are estimated. To test this possibility we consider 5 additional starting models for the deterministic inversion of the base data. Table 3 presents the characteristics of these models. The first three models are built from the mean estimates of the 1-D MCMC inversions presented in Section 4.1. The fourth and fifth model are based on the 4-layer model previously used but present two unconnected conductors and a conductive layer, respectively, at the injection depth. The unconnected conductors are oriented in the north–south direction, they are separated by ~ 2 km and are located on opposite sides of the injection point. They have a vertical extension of ~ 5 km and are completely embedded in the layer with resistivity of $550 \Omega\text{m}$.

The deterministic inversions based on these starting models provide new base models that fit the base data to similar levels as the original one. We then compute the time-lapse data using the residuals of each model and run new resistivity-difference-based probabilistic time-lapse inversions until a stable data misfit level is reached. Note that no formal convergence of the chains was reached due to computational constraints and therefore these estimates are used only to qualitatively assess the variations due to different base

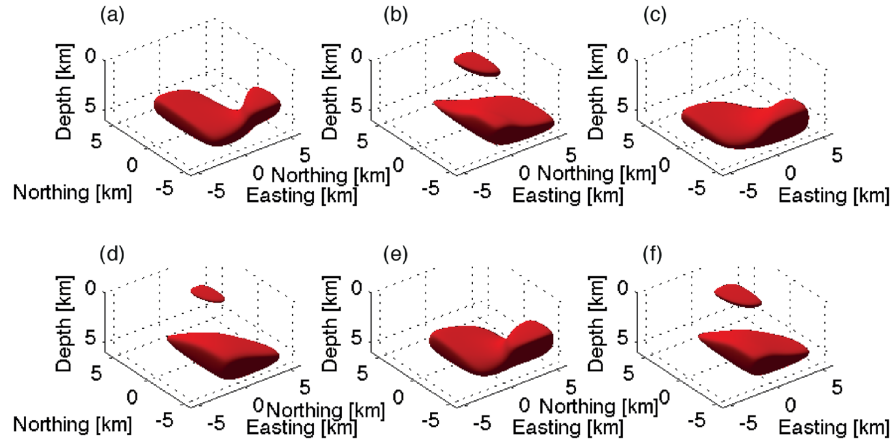


Figure 12. (a–f) Random posterior realizations from the resistivity-difference-based MCMC inversion of the Paralana time-lapse data. The isosurfaces correspond to a value of $\theta = 10^{-7}$.

Table 3. Initial structure and resulting resistivity change and spread ratio estimates of the 1-D models used to test the influence of the base model. The letters ‘ r ’ and ‘ h ’ correspond to the layer resistivity and thickness, respectively.

Conceptual model	1st layer (top)	2nd layer	3rd layer	4th layer	5th layer	6th layer	$\Delta \log_{10} r_{\max}$	S_{xx}/S_{yy}
Half-space	–	–	–	–	–	–	–5.8	1.1
	$r_1 = 8 \Omega\text{m}$	–	–	–	–	–		
2 layers	$h_1 = 594 \text{ m}$	–	–	–	–	–	–8.5	1.1
	$r_1 = 4 \Omega\text{m}$	$r_2 = 46 \Omega\text{m}$	–	–	–	–		
3 layers	$h_1 = 55 \text{ m}$	$h_2 = 430 \text{ m}$	–	–	–	–	–7.2	1.4
	$r_1 = 9.6 \Omega\text{m}$	$r_2 = 3.3 \Omega\text{m}$	$r_3 = 45 \Omega\text{m}$	–	–	–		
4 layers with 2 unconnected conductors	$h_1 = 33 \text{ m}$	$h_2 = 700 \text{ m}$	$h_3 = 7780 \text{ m}$	–	–	–	–6.6	1.2
	$r_1 = 70 \Omega\text{m}$	$r_2 = 4 \Omega\text{m}$	$r_3 = 550 \Omega\text{m}$	$r_4 = 20 \Omega\text{m}$	–	–		
6 layers	$h_1 = 33 \text{ m}$	$h_2 = 700 \text{ m}$	$h_3 = 2650 \text{ m}$	$h_4 = 1520 \text{ m}$	$h_5 = 3610 \text{ m}$	–	–9.0	1.4
	$r_1 = 70 \Omega\text{m}$	$r_2 = 4 \Omega\text{m}$	$r_3 = 550 \Omega\text{m}$	$r_4 = 55 \Omega\text{m}$	$r_5 = 550 \Omega\text{m}$	$r_6 = 20 \Omega\text{m}$		

models. Table 3 shows the estimated maximum resistivity changes $\Delta \log_{10} r_{\max}$ and horizontal spread ratio S_{xx}/S_{yy} for each base model. Large differences can be observed among the maximum changes, which give evidence of the influence of the base model on the estimation of the time-lapse changes. For example, the maximum resistivity change in the plume area is estimated in –5.8 when the base model is derived from a half-space, and it is of –9.0 when a 6-layer model is used. Nonetheless, all the estimates point to a plume more elongated in the north–south direction than in the east–west direction. Note that all the models resulting from these inversions explain the data to the same level as the resistivity-difference-based inversion presented in the previous section (*cf.* Table 2).

6 DISCUSSION

Our results indicate that it is possible to infer information about tracer plumes in deep injection experiments using MT data, but also that many important challenges remain. Our probabilistic time-lapse inversion methodology has several advantages over the deterministic approach. The non-linearity of the inverse problem is correctly treated and the uncertainty of the model parameters is formally characterized. Furthermore, valuable prior information such as the injection depth, the electrical resistivity expected only to decrease or stay unchanged after the saline injection, and bounds on the region where resistivity can decrease, can be flexibly implemented in the MCMC inversion. The results of the synthetic example shown in Figs 8–10 suggest that our approach works properly when the

base resistivity model is suitable, and the plume is in accordance with the proposed physical model. The MCMC inversion correctly retrieves the change in the cementation factor and the centre of mass and spread of the plume. Higher orders of the Legendre moment decomposition could be used, which would allow for more complicated 3-D structures (*cf.* Laloy *et al.* 2012). The computational costs would then also be larger (3 months were needed for the inversion of the Paralana data to converge for Legendre moments up to order 3), but it is unlikely that smaller details would be resolved.

The large time-lapse changes observed in the MT data following the injection experiment in Paralana were used by Peacock *et al.* (2013) to derive qualitative information about the direction of flow of the injected fluids. Our deterministic 3-D time-lapse inversion was useful to determine the geographical regions of maximum resistivity changes, even if the inferred changes in depth appear to be too shallow. These changes were located above the actual injection point and towards the south and the west. The depth of the anomaly may be a result of the higher sensitivity of the inversion at shallower depths but could also be related to an inadequate base model. Unphysical increases in resistivity also appear (see Fig. 7) as no constraints regarding the sign of the resistivity changes were applied. Including these types of constraints could help to improve the deterministic inversions. For example, penalizing positive changes in the resistivity model and using an l_1 -norm to penalize the model structure would lead to more compact resistivity changes (see examples for 2-D inversions in Rosas Carbajal *et al.* 2012).

Very large resistivity changes were needed to explain the Paralana time-lapse data. For example, the amount of injected water had to be increased and the depth of injection moved to shallower depths to obtain similar time-lapse changes for the synthetic example. An inversion of the Paralana data using our upscaling and petrophysical model that accounted for the amount of saline water injected could not explain the data changes. This suggests limitations of the petrophysical model used and raises the question of whether changes in reservoir properties can be inferred from the time-lapse MT data. In this regard, Vasco *et al.* (2014) argue that instead of aiming at relating changes in geophysical properties to changes in reservoir properties, it may be more viable to relate the initiation of a change in a geophysical property to key reservoir changes such as fluid saturation or pressures. While Vasco *et al.* (2014) consider reservoir monitoring with seismic data, the application to MT data where relatively long time series have to be used to obtain good signal-to-noise ratios of the transfer functions is not straightforward.

When directly inferring the changes in resistivity, while keeping constraints on the location of the plume (injection depth and limited spatial dimensions), the probabilistic inversion could fit the data and retrieved water plumes that are more elongated in the north–south direction. Compared to the microseismics, the centre of mass of the plume is located to the south of the injection point, and the plumes predicted from the MT data are much larger in extent (see Fig. 12). The latter is expected, as the microseismic data sense the opening of fractures whereas the MT time-lapse data sense changes in electrical resistivity, which happen where the injected fluid is present and not only where fractures open. Also, the microseismic data were measured during the injection, while the time-lapse MT data were acquired one week after the injection was completed.

To evaluate the influence of the base model, we performed time-lapse inversions using different base models that equally explain the base data. The discrepancy observed between the plume estimates calculated with different base models suggests that, to a large extent, the large resistivity changes needed to explain the time-lapse data are related to our chosen base model. The base model derived from a half-space resulted in the smallest maximum resistivity change, with a log-value of -5.8 (cf. Table 3). That is, in order to explain the time-lapse data, a resistivity change with respect to the base model of more than five orders of magnitude is needed. The fact that the other base models require larger resistivity changes to explain the data may be a consequence of the conductive surface layer they all contain, which reduces the sensitivity to deeper resistive layers. This does not mean that the half-space-like base model is the most appropriate. Its resistivity value ($8 \Omega\text{m}$) and MT response as compared to the base data do not appear realistic. Most likely, none of the evaluated base models include the correct heterogeneity distributions that would lead to the true resistivity changes needed to explain the time-lapse data. The synthetic example, which was performed using the correct base model, yielded satisfactory estimates of the plume. To further constrain the model, one could perform a time-lapse MCMC inversion where both the base model heterogeneities and the plume geometry would be inverted for at the same time, minimizing the resistivity changes involved. Such methods have been proposed for deterministic time-lapse studies involving ERT data (Kim *et al.* 2009; Karaoulis *et al.* 2011). This type of study would be highly computationally demanding, and we leave it for future investigations.

The extremely large resistivity changes needed to explain the time-lapse data raise important questions about how such a large conductance anomaly could be caused by the injection. Surface

conductivity could not explain the changes even if clay minerals were present as its effect would be decreased by the injected conductive water. One possibility is that, as the rock dissolves due to the injected acids, more minerals are incorporated into the fluids and thus the salinity of the fluid increases, therefore decreasing the bulk resistivity. Another alternative is that the large changes observed originated from the presence of microscopic or macroscopic electrical anisotropy. The latter could be the result of a complex arrangement of fractures, which in some directions were effectively connected by the fracture stimulation whereas in other directions stay in the vicinity of the percolation threshold. Such situations were suggested by Bahr (2000) to explain the distortion in MT data and by Hautot *et al.* (2002) to associate observed temporal variations in resistivity to pore pressure changes controlled by lake level variations. Reid *et al.* (2011) reported on high fluid pressures encountered when drilling the Paralana borehole and after the injection experiment was finished. This supports the hypothesis that fractures may be well connected in some directions while staying close to the percolation threshold in others, thus creating large variations of the measured electric fields. Simulating the MT responses of realistic complex fracture networks would be highly computationally demanding and it is out of the scope of this contribution.

7 CONCLUSIONS

We presented the first time-lapse 3-D deterministic and probabilistic inversions of MT data, with focus on imaging a tracer plume created by injecting a saline tracer in a geothermal system. The time-lapse deterministic inversion resulted in resistivity changes that are much shallower than the depth of the injection, which demonstrates the importance of including prior information such as the injection point and that the electrical resistivity is expected to decrease following the injection. The probabilistic approach used relied on petrophysical relations and a reduced Legendre moment decomposition of the injected plume that decreases the parameter dimensionality and thus the computation times. This approach was effective when applied to a synthetic test case. For the inversion of the Paralana data, the applied petrophysical relation and upscaling procedure were not able to explain the large data changes observed and a resistivity-difference-based inversion with relaxed constraints had to be used. The plumes belonging to the posterior pdf are elongated in the north–south direction, which is in agreement with microseismic data. However, their centre of mass is estimated to be located south from the injection point, which is in contrast to the microseismic events, and the inferred resistivity changes are extremely large (many orders of magnitude larger than expected). Since the studied media is highly fractured, a possible explanation for the large resistivity changes is the existence of a connected fracture network that is close to the percolation threshold in one direction. Another related possibility is a heterogeneous resistivity distribution that is poorly represented by our smoothly varying base model. A simple analysis using different base models supports this explanation. Thus, more efforts have to be put in the accurate characterization of the base model when performing monitoring studies with EM methods.

ACKNOWLEDGEMENTS

We thank Eric Laloy for his advice on the use of the Legendre moment parametrization, Philippe Logean for his help with the cluster implementations, Damien Jougnot for useful discussions about petrophysics, Anna Kelbert and Gary Egbert for providing

the ModEM program for the deterministic inversions and forward computations, Jasper Vrugt for providing the DREAM_(ZS) program and two anonymous reviewers and the Editor Ute Weckmann for their constructive comments. This work was supported by the Swiss National Science Foundation under grants 200021-130200 and 200020-149117.

REFERENCES

- Aizawa, K., Kanda, W., Ogawa, Y., Iguchi, M., Yokoo, A., Yakiwara, H. & Sugano, T., 2011. Temporal changes in electrical resistivity at Sakurajima volcano from continuous magnetotelluric observations, *J. Volc. Geotherm. Res.*, **199**(1), 165–175.
- Ajo-Franklin, J.B., Minsley, B.J. & Daley, T.M., 2007. Applying compactness constraints to differential traveltime tomography, *Geophysics*, **72**(4), R67–R75.
- Archie, G., 1942. The electrical resistivity log as an aid in determining some reservoir characteristic, *Trans. Am. Instit. Min. Metall. Eng.*, **146**, 54–62.
- Bahr, K., 2000. Percolation in the crust derived from distortion of electric fields, *Geophys. Res. Lett.*, **27**(7), 1049–1052.
- Bedrosian, P.A., Weckmann, U., Ritter, O., Hammer, C.U., Hübert, J. & Jung, A., 2004. Electromagnetic monitoring of the Groß Schönebeck stimulation experiment, in *Jahrestagung der Deutschen Geophysikalischen Gesellschaft*, vol. 64, GFZ, Berlin.
- Brace, W., Orange, A. & Madden, T., 1965. Effect of pressure on the electrical resistivity of water-saturated crystalline rocks, *J. geophys. Res.*, **70**, 5669–5678.
- Brenguier, F., Shapiro, N.M., Campillo, M., Nercessian, A. & Ferrazzini, V., 2007. 3-D surface wave tomography of the Piton de la Fournaise volcano using seismic noise correlations, *Geophys. Res. Lett.*, **34**(2), doi:10.1029/2006GL028586.
- Brenguier, F., Shapiro, N.M., Campillo, M., Ferrazzini, V., Duputel, Z., Coutant, O. & Nercessian, A., 2008. Towards forecasting volcanic eruptions using seismic noise, *Nat. Geosci.*, **1**(2), 126–130.
- Brugger, J., Long, N., McPhail, D. & Plimer, I., 2005. An active amagmatic hydrothermal system: the Paralana hot springs, Northern Flinders Ranges, South Australia, *Chem. Geol. (Isot. Geosci. Sect.)*, **222**(1), 35–64.
- Chave, A.D. & Thomson, D.J., 1989. Some comments on magnetotelluric response function estimation, *J. geophys. Res.*, **94**(B10), 14 215–14 225.
- Chen, J., Hoversten, G.M., Vasco, D., Rubin, Y. & Hou, Z., 2007. A Bayesian model for gas saturation estimation using marine seismic AVA and CSEM data, *Geophysics*, **72**(2), WA85–WA95.
- Chen, J., Hoversten, G.M., Key, K., Nordquist, G. & Cumming, W., 2012. Stochastic inversion of magnetotelluric data using a sharp boundary parameterization and application to a geothermal site, *Geophysics*, **77**(4), E265–E279.
- Claerbout, J.F. & Muir, F., 1973. Robust modeling with erratic data, *Geophysics*, **38**(5), 826–844.
- Constable, S., 2010. Ten years of marine csem for hydrocarbon exploration, *Geophysics*, **75**(5), A67–A81.
- Day-Lewis, F.D., Harris, J.M. & Gorelick, S.M., 2002. Time-lapse inversion of crosswell radar data, *Geophysics*, **67**(6), 1740–1752.
- Doetsch, J., Linde, N. & Binley, A., 2010. Structural joint inversion of time-lapse crosshole ERT and GPR traveltime data, *Geophys. Res. Lett.*, **37**(24), L24404, doi:10.1029/2010GL045482.
- Egbert, G.D. & Booker, J.R., 1986. Robust estimation of geomagnetic transfer functions, *Geophys. J. Int.*, **87**(1), 173–194.
- Egbert, G.D. & Kelbert, A., 2012. Computational recipes for electromagnetic inverse problems, *Geophys. J. Int.*, **189**(1), 251–267.
- Falgàs, E., Ledo, J., Marcuello, A. & Queralt, P., 2009. Monitoring freshwater-seawater interface dynamics with audiomagnetotelluric data, *Near Surface Geophysics*, **7**(5–6), 391–399.
- Farquharson, C.G. & Oldenburg, D.W., 1998. Non-linear inversion using general measures of data misfit and model structure, *Geophys. J. Int.*, **134**(1), 213–227.
- Gelman, A. & Rubin, D.B., 1992. Inference from iterative simulation using multiple sequences, *Statistical Science*, **7**, 457–472.
- Grandis, H., Menvielle, M. & Roussignol, M., 1999. Bayesian inversion with Markov chains: I. The magnetotelluric one-dimensional case, *Geophys. J. Int.*, **138**(3), 757–768.
- Grandis, H., Menvielle, M. & Roussignol, M., 2002. Thin-sheet electromagnetic inversion modeling using Monte Carlo Markov Chain (MCMC) algorithm, *Earth Planets Space*, **54**(5), 511–522.
- Grayver, A.V., Streich, R. & Ritter, O., 2014. 3D inversion and resolution analysis of land-based CSEM data from the Ketzin CO₂ storage formation, *Geophysics*, **79**(2), E101–E114.
- Hasting, M. *et al.*, 2011. Real-time induced seismicity monitoring during wellbore stimulation at Paralana-2 South Australia in *Australian Geothermal Energy Conference*, 16–18 November, Melbourne, Australia.
- Hautot, S., Tarits, P., Perrier, F., Tarits, C. & Trique, M., 2002. Ground-water electromagnetic imaging in complex geological and topographical regions: a case study of a tectonic boundary in the French Alps, *Geophysics*, **67**(4), 1048–1060.
- Hou, Z., Rubin, Y., Hoversten, G.M., Vasco, D. & Chen, J., 2006. Reservoir-parameter identification using minimum relative entropy-based Bayesian inversion of seismic AVA and marine CSEM data, *Geophysics*, **71**(6), O77–O88.
- House, L., 1987. Locating microearthquakes induced by hydraulic fracturing in crystalline rock, *Geophys. Res. Lett.*, **14**(9), 919–921.
- Hubbard, S.S. & Rubin, Y., 2005. Introduction to hydrogeophysics, in *Hydrogeophysics*, pp. 3–21, Springer.
- Jougnot, D. & Revil, A., 2010. Thermal conductivity of unsaturated clay-rocks, *Hydrology and Earth System Sciences*, **14**(1), 91–98.
- Kappler, K., Morrison, H.F. & Egbert, G., 2010. Long-term monitoring of ULF electromagnetic fields at Parkfield, California, *J. geophys. Res.*, **115**(B4), doi:10.1029/2009JB006421.
- Karaoulis, M., Kim, J.-H. & Tsourlos, P., 2011. 4D active time constrained resistivity inversion, *J. appl. Geophys.*, **73**(1), 25–34.
- Khan, A., Connolly, J. & Olsen, N., 2006. Constraining the composition and thermal state of the mantle beneath Europe from inversion of long-period electromagnetic sounding data, *J. geophys. Res.*, **111**(B10), doi:10.1029/2006JB004270.
- Kim, J.-H., Yi, M.-J., Park, S.-G. & Kim, J.G., 2009. 4-D inversion of DC resistivity monitoring data acquired over a dynamically changing earth model, *J. Appl. Geophys.*, **68**(4), 522–532.
- LaBrecque, D.J. & Yang, X., 2001. Difference inversion of ERT data: A fast inversion method for 3-D in situ monitoring, *J. Environ. Eng. Geophys.*, **6**(2), 83–89.
- Laloy, E. & Vrugt, J.A., 2012. High-dimensional posterior exploration of hydrologic models using multiple-try DREAM (ZS) and high-performance computing, *Water Resour. Res.*, **48**(1), doi:10.1029/2011WR010608.
- Laloy, E., Linde, N. & Vrugt, J., 2012. Mass conservative three-dimensional water tracer distribution from Markov chain Monte Carlo inversion of time-lapse ground-penetrating radar data, *Water Resour. Res.*, **48**(7), W07510, doi:10.1029/2011WR011238.
- Lien, M. & Mannseth, T., 2008. Sensitivity study of marine CSEM data for reservoir production monitoring, *Geophysics*, **73**(4), F151–F163.
- Linde, N. & Pedersen, L.B., 2004. Evidence of electrical anisotropy in limestone formations using the RMT technique, *Geophysics*, **69**(4), 909–916.
- Linde, N. & Vrugt, J.A., 2013. Distributed soil moisture from crosshole ground-penetrating radar travel times using stochastic inversion, *Vadose Zone J.*, **12**(1), doi:10.2136/vzj2012.0101.
- Lochbühler, T., Breen, S.J., Detwiler, R.L., Vrugt, J.A. & Linde, N., 2014. Probabilistic electrical resistivity tomography of a CO₂ sequestration analog, *J. Appl. Geophys.*, **107**, 80–92.
- Menke, W., 1989. *Geophysical Data Analysis: Discrete Inverse Theory*, Academic Press.
- Miller, C.R., Routh, P.S., Brosten, T.R. & McNamara, J.P., 2008. Application of time-lapse ERT imaging to watershed characterization, *Geophysics*, **73**(3), G7–G17.
- Mosegaard, K. & Tarantola, A., 1995. Monte Carlo sampling of solutions to inverse problems, *J. geophys. Res.*, **100**(B7), 12 431–12 447.
- Muñoz, G., 2014. Exploring for geothermal resources with electromagnetic methods, *Surv. Geophys.*, **35**(1), 101–122.

- Neumann, N., Sandiford, M. & Foden, J., 2000. Regional geochemistry and continental heat flow: implications for the origin of the South Australian heat flow anomaly, *Earth planet. Sci. Lett.*, **183**(1), 107–120.
- Nocedal, J. & Wright, S.J., 2006. *Conjugate Gradient Methods*, Springer.
- Orange, A., Key, K. & Constable, S., 2009. The feasibility of reservoir monitoring using time-lapse marine CSEM, *Geophysics*, **74**(2), F21–F29.
- Peacock, J.R., Thiel, S., Reid, P. & Heinson, G., 2012. Magnetotelluric monitoring of a fluid injection: example from an enhanced geothermal system, *Geophys. Res. Lett.*, **39**(18), doi:10.1029/2012GL053080.
- Peacock, J.R., Thiel, S., Heinson, G.S. & Reid, P., 2013. Time-lapse magnetotelluric monitoring of an enhanced geothermal system, *Geophysics*, **78**(3), B121–B130.
- Ramirez, A.L. et al., 2005. Stochastic inversion of electrical resistivity changes using a Markov Chain Monte Carlo approach, *J. geophys. Res.*, **110**(B2), doi:10.1029/2004JB003449.
- Reid, P., Messeiller, M. & Llanos, E., 2011. Paralana EGS project-findings from the fracture stimulation, in *Australian Geothermal Energy Conference*, 16–18 November, Melbourne, Australia.
- Roberts, G.O. & Rosenthal, J.S., 2007. Coupling and ergodicity of adaptive Markov chain Monte Carlo algorithms, *J. Appl. Probab.*, **44**(2), 458–475.
- Rosas Carbajal, M., Linde, N. & Kalscheuer, T., 2012. Focused time-lapse inversion of radio and audio magnetotelluric data, *J. Appl. Geophys.*, **84**, 29–38.
- Rosas-Carbajal, M., Linde, N., Kalscheuer, T. & Vrugt, J.A., 2014. Two-dimensional probabilistic inversion of plane-wave electromagnetic data: methodology, model constraints and joint inversion with electrical resistivity data, *Geophys. J. Int.*, **196**(3), 1508–1524.
- Sambridge, M. & Mosegaard, K., 2002. Monte Carlo methods in geophysical inverse problems, *Rev. Geophys.*, **40**(3), 3–1.
- Sen, P.N. & Goode, P.A., 1992. Influence of temperature on electrical conductivity on shaly sands, *Geophysics*, **57**(1), 89–96.
- Streich, R. & Becken, M., 2011. Electromagnetic fields generated by finite-length wire sources: comparison with point dipole solutions, *Geophys. Prospect.*, **59**, 361–374.
- Tarantola, A., 2005. *Inverse Problem Theory and Methods for Model Parameter Estimation*, SIAM.
- Tarantola, A. & Valette, B., 1982. Inverse problems = quest for information, *J. Geophys.*, **50**(3), 150–170.
- Tarits, P., Jouanne, V., Menvielle, M. & Roussignol, M., 1994. Bayesian statistics of non-linear inverse problems: example of the magnetotelluric 1-D inverse problem, *Geophys. J. Int.*, **119**(2), 353–368.
- Teague, M.R., 1980. Image analysis via the general theory of moments, *J. Opt. Soc. Am.*, **70**(8), 920–930.
- Vasco, D., Daley, T.M. & Bakulin, A., 2014. Utilizing the onset of time-lapse changes: a robust basis for reservoir monitoring and characterization, *Geophys. J. Int.*, **197**(1), 542–556.
- Wirianto, M., Mulder, W. & Slob, E., 2010. A feasibility study of land CSEM reservoir monitoring in a complex 3-D model, *Geophys. J. Int.*, **181**(2), 741–755.